

Nanoelectronic and nanomechanical systems

J.S. Aldridge, R. Knobel,

D.R. Schmidt, C.S. Yung and A.N. Cleland *

Department of Physics and iQUEST, University of California at Santa Barbara, Santa Barbara CA 93106

(Dated: September 20, 2001)

Nanomechanical systems, integrated with nanoelectronic transducers and sensors, are in an early stage of development. Research is focused on the development of radiofrequency mechanical resonators, sensitive electrometers and magnetometers, and potentially quantum-limited energy and motion sensors. This paper will review the current state of our efforts in this area, and will describe research in which the integration of mechanics and electronics will potentially allow the demonstration of macroscopic quantum effects in mechanical systems. We are particularly interested in observing and measuring quantum-limited systems, whose behavior is strongly affected by the measurement system; such systems may provide further insight into the quantum measurement process.

Keywords: Nanomechanics, nanoelectronics, single electron transistor, bolometer

We are developing a number of novel approaches for the integration of electrical systems with the mechanical degrees of freedom in nanometer-scale structures. Our central theme is to unify the very sensitive characteristics of tunnel junctions with mechanically suspended structures. Projects underway include the development of a nanoscale bolometer comprising a suspended structure with a very small heat capacity, weakly linked to the environment, mechanically suspended beams with an integrated two-dimensional electron gas, and flexural resonators electrically coupled to single electron transistors, which act as displacement sensors.

I. FLEXURAL RESONATORS

Flexural resonators, either in the form of cantilevers or doubly-clamped beams, form a basic element in nanomechanical structures. A doubly-clamped resonator with thickness t and length L has a fundamental flexural resonance frequency given by

$$\frac{\Omega_0}{2\pi} = 1.027 \sqrt{\frac{E}{\rho}} \frac{t}{L^2}. \quad (1)$$

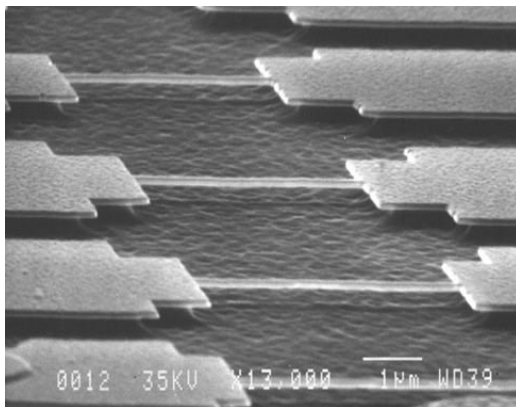


FIG. 1: Series of four AlN beams, with the undercut lengths ranging from 3.9 to 5.6 μm . The beams are 0.17 μm thick, and the widths are 0.2 μm , increasing to widths of 2.4 μm at either end.

* Corresponding author: E-mail: cleland@physics.ucsb.edu

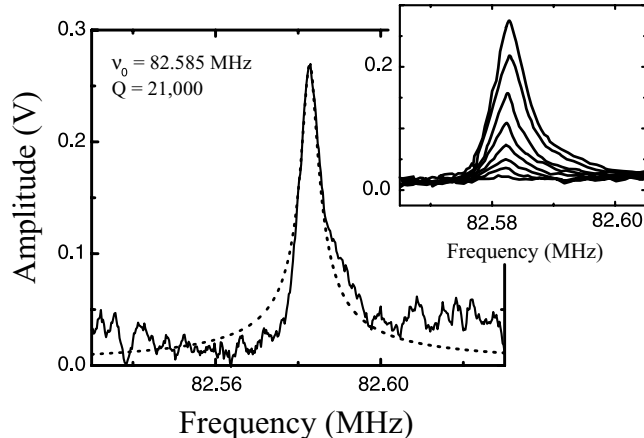


FIG. 2: Measured resonance of a $3.9 \mu\text{m}$ long beam, measured at 4.2 K in a transverse magnetic field of 8 T. Applied rf power was -85 dBm. *Inset*: Measured resonance for a constant rf power of -75 dBm, while varying the magnetic field through integer values from 1 T (smallest peak) to 8 T (largest peak).

A beam fabricated from Si with thickness $t = 0.2 \mu\text{m}$ and a length of $100 \mu\text{m}$ has a resonance frequency of about 170 kHz; shortening the length to $10 \mu\text{m}$ increases the frequency to 17 MHz, and a further reduction to $1 \mu\text{m}$ brings the frequency up to 1.7 GHz. Quality factors for the fundamental resonance have been measured in excess of 20,000 [1, 2]. Such resonators form candidates as stable local oscillators for time-base and frequency standards applications [3, 4].

These structures are coupled to external electronic circuitry using a number of methods: through magnetomotive transduction, through electrostatic displacement sensing and actuation, and through the piezoelectric effect. The magnetomotive technique [1, 5] involves placing the mechanically active element in a transverse magnetic field, and passing a current through a metal film integrated with the mechanical structure. A Lorentz force develops as a result, generating a displacement; the displacement then generates an electromotive voltage, which can be sensed using external electronics.

In Fig. 1 we show a set of flexural beams fabricated from single-crystal aluminum nitride. We have been developing this material because of its low density, high elastic modulus, and relatively high fracture strength. This material can be grown as single crystal films on (111)-orientation Si wafers using metal-organic chemical-vapor deposition. The films can subsequently be patterned using a combination of electron beam lithography and thin metal film deposition. The AlN can be anisotropically etched using Cl_2 -based reactive ion etching, and the substrate Si selectively removed using an isotropic Si etch (ammonium fluoride, nitric acid and water). More fabrication details are discussed below.

The structures shown in Fig. 1 were measured using the magnetomotive technique; a series of resonance curves is shown in Fig. 2. Resonance frequencies have been measured [2] in the range of 40-80 MHz, with quality factors measured to be somewhat higher than 20,000.

The electrostatic approach involves the use of displaceable capacitors, where a voltage applied across the plates of a mechanically flexible capacitor causes one plate to displace with respect to the other. The displacement can be detected by monitoring the resulting change in capacitance [3]. An example of a nanoscale structure with electrostatic drive and sense, fabricated from single-crystal Si using a silicon-on-insulator substrate as the base material, is shown in Fig. 3.

II. SET-BASED DISPLACEMENT SENSING

We are attempting to develop a potentially quantum-limited displacement sensing approach, based on the single-electron transistor (SET). The structure we are fabricating comprises a doubly-clamped flexural beam, coupled through a capacitive, mechanically variable capacitor to the gate lead of the SET. A micrograph of a completed structure, with doubly-clamped beam and adjacent single-electron transistor, is shown in Fig. 4. The

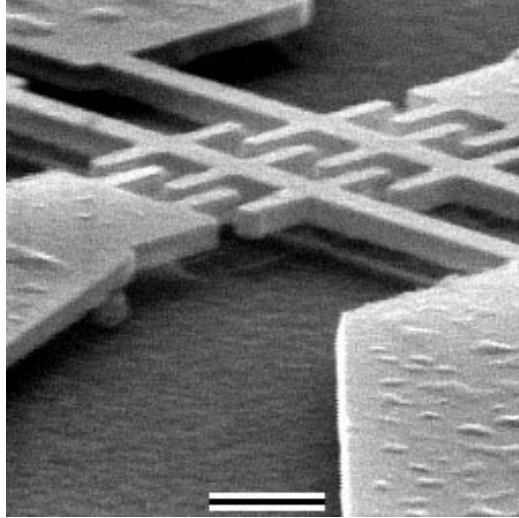


FIG. 3: Single-crystal silicon flexural resonators coupled by capacitive transducers, allowing both displacement actuation and sensing. The horizontal scale bar is 1 μm . The flexural resonance frequency of these structures is measured to be 68 MHz.

mechanical beam can be driven using an external signal, using magnetomotive displacement; it will also exhibit thermally-driven fluctuations due to its finite value of damping, parameterized by the quality factor Q . Further, as discussed below, we expect the beam to exhibit motion driven by the back-action measurement noise from the SET. The beam can be biased with a dc voltage V_0 , which induces a coupling charge on the capacitor; motion of the beam changes the charge coupled to the single-electron transistor, modulating the drain-source current in the transistor.

In a recent innovation [6], the SET can be used as a radio-frequency electrometer, for which the input charge noise has been measured to be about $2 \times 10^{-5} e/\sqrt{\text{Hz}}$. There has been a proposal to use the SET as a displacement sensor [7], estimating the displacement sensitivity when it is coupled to a radiofrequency resonator, and a recent estimate of the magnitude of the electrical back action generated by the SET on the resonator [8].

The displacement of the resonator is sensed by changes in the coupling capacitance C_c and the corresponding coupled charge. The sensitivity of the SET as a displacement sensor is determined by its charge sensitivity, by the sensitivity of the coupling capacitance on the resonator displacement, and by the magnitude of the SET back-action on the mechanical resonator. The back-action is caused by the force exerted on the resonator when the voltage on the center island of the SET fluctuates. This can be evaluated as follows: The electrostatic charging energy of the coupling capacitance is $\varepsilon = C_c V_c^2/2$, where $C_c(x)$ is the position-dependent capacitance, and x is the displacement at the midpoint of the resonator; the voltage V_c is the voltage across the coupling capacitor. This voltage consists of the externally-imposed voltage V_0 and a noise voltage δV , which fluctuates due to the stochastic nature of electron flow through the SET.

The electrostatic force generated by V_c is given by $F = d\varepsilon/dx = (V_c^2/2)dC_c/dx$. A fluctuation δV in the voltage V_c gives rise to a fluctuation δF in the force through

$$\delta F = V_0 \frac{dC_c}{dx} \delta V, \quad (2)$$

where V_0 is the constant value of V_c .

Following Schwab [8], the noise voltage δV can be evaluated using the amplifier noise model developed for the SET by Devoret and Schoelkopf [9]. It has a spectral density due to the SET input current noise $S_I(\omega)$ driving the coupling capacitance C_c , given by $S_I(\omega)/\omega^2 C_c^2$. The spectral noise density $S_F(\omega)$ of the force on the resonator is then given by

$$S_F(\omega) = \left(V_0 \frac{dC_c}{dx} \right)^2 \frac{S_I(\omega)}{\omega^2 C_c^2(x)}, \quad (3)$$

An optimized SET, with both tunnel junction resistances equal to the quantum of resistance $h/e^2 \approx 25 \text{ k}\Omega$, has a current noise that at low frequencies is approximately given by

$$S_I(\omega) = \frac{5}{9} \frac{C_c^2(x)}{C_\Sigma} h\omega^2, \quad (4)$$

where C_Σ is the total capacitance of the SET island.

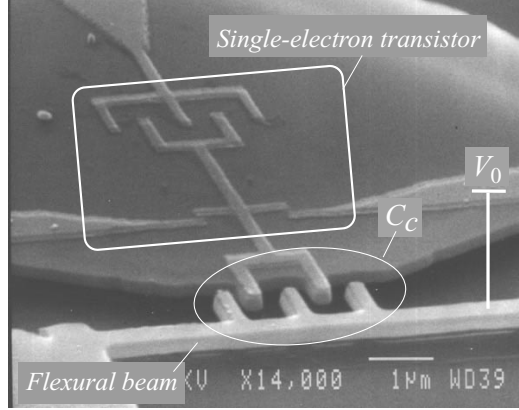


FIG. 4: Electron micrograph of a doubly-clamped beam coupled to a single-electron transistor. The resonating beam includes an interdigitated capacitor $C_c(x)$ coupled to the gate of the single-electron transistor; the displacement x of the beam center point changes the coupled charge, and modulates the current through the transistor. The beam can be biased with a dc voltage V_0 .

The displacement spectral density $S_x(\omega)$ may then be evaluated using the response function of the resonator; for a resonator with mass M , resonance frequency Ω_0 and quality factor Q , this is related to the force spectral density $S_F(\omega)$ by

$$S_x(\omega) = \frac{1}{(\Omega_0^2 - \omega^2)^2 + (\omega_0^2/Q)^2} \frac{S_F(\omega)}{M^2\Omega_0^4}. \quad (5)$$

For a high quality factor resonator, with $Q \gg 1$, the response (5) is very narrow-band, so the spectral density of the force (3) may be taken to be frequency-independent, with $S_I(\omega)$ evaluated at $\omega = \Omega_0$.

The back-action noise of the SET can now be re-stated as an effective noise temperature: The dissipation associated with a finite value of the quality factor Q generates a fluctuating force of magnitude [4]

$$S_F(\omega) = \frac{2k_B T_{\text{eff}} M \Omega_0}{\pi Q}, \quad (6)$$

where T_{eff} is the temperature; this relation is determined by the fluctuation-dissipation theorem. For the SET, we therefore can define an effective noise temperature

$$T_{\text{eff}} = \frac{5\pi}{18k_B} \frac{QV_0^2}{M\Omega_0} \left(\frac{dC_c}{dx} \right)^2 \frac{h}{C_\Sigma}. \quad (7)$$

In addition to the SET-driven noise, the resonator has a physical temperature T , so in the classical limit $k_B T \gg \hbar\Omega_0$, the total noise amplitude of motion corresponds to a temperature $T + T_{\text{eff}}$.

This motion is sensed by the SET, with a displacement sensitivity determined by the coupling of the resonator to the SET and the SET input voltage noise $S_V(\omega)$. The voltage noise for an optimized SET is given by

$$S_V(\omega) = \frac{65hC_\Sigma}{288C_c^2(x)}, \quad (8)$$

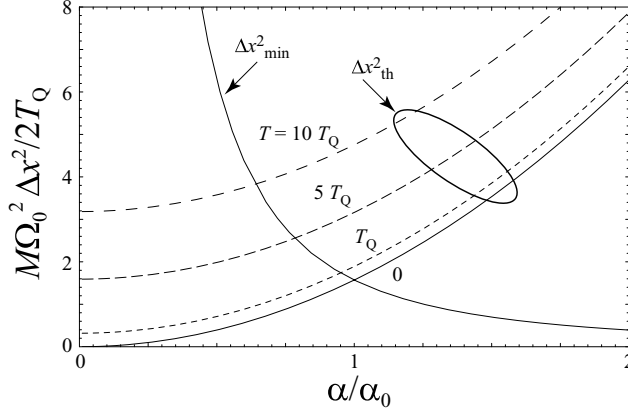


FIG. 5: Displacement noise energy as a function of coupling strength α/α_0 , for different resonator temperatures in units of the temperature quantum $T_Q = \hbar\Omega_0$. The optimal coupling is achieved when the minimum displacement energy is equal to the thermal energy.

and is approximately white. Referring the voltage noise as a effective displacement noise $S_{x\text{eff}}$, we have

$$S_{x\text{eff}}(\omega) = \left(\frac{C_c(x)}{V_0} \frac{1}{dC_c/dx} \right)^2 S_V(\omega) \approx \frac{\hbar C_\Sigma}{4V_0^2 (dC_c/dx)^2}. \quad (9)$$

The thermally-driven displacement has a frequency spectrum concentrated in the band centered on Ω_0 with a width $\Delta\Omega = 2\Omega_0/Q$; integrating the noise power over this band, we find a mean square noise

$$\Delta x_{\text{th}}^2 = \int_{\Delta\Omega} S_x(\omega) d\omega \approx 1.11 \frac{2k_B(T + T_{\text{eff}})}{\pi M\Omega_0^2}. \quad (10)$$

The input displacement noise of the SET integrated over the same band gives a minimum detectable square displacement

$$\Delta x_{\text{min}}^2 = S_{x\text{eff}} \Delta\Omega = \frac{\hbar\Omega_0 C_\Sigma}{2QV_0^2 (dC_c/dx)^2}. \quad (11)$$

The coupling strength $\alpha = V_0 dC_c/dx$ can be tuned by adjusting the dc voltage V_0 ; increasing the voltage reduces the minimum detectable displacement Δx_{min} , but also increases the effective temperature T_{eff} . At zero resonator physical temperature $T = 0$, the optimum coupling α_0 is achieved when $\Delta x_{\text{th}} = \Delta x_{\text{min}}$, or when

$$\alpha_0 = V_0 \frac{dC_c}{dx} = \sqrt{\frac{M\Omega_0^2 C_\Sigma}{Q}}. \quad (12)$$

At this optimal bias point, the minimum displacement noise is $\Delta x_{\text{min}}^2 = \hbar/2M\Omega_0$, close to that given by the standard quantum limit of $\hbar/2M\Omega_0$. Taking a model resonator of $\Omega_0 = 2\pi \times 10^8$ Hz, mass $M = 3 \times 10^{-16}$ kg, the rms displacement noise is 4×10^{-14} m.

At non-zero resonator temperatures, the optimal coupling value α decreases. In Fig. 5 we show the dependence of the thermal and back action-driven displacement energy $M\Omega_0^2\Delta x_{\text{th}}^2/2$, and the corresponding detectable energy $M\Omega_0^2\Delta x_{\text{min}}^2/2$, as a function of coupling strength. The thermal energy is calculated for a number of resonator temperatures, in units of the quantum temperature $T_Q = \hbar\Omega_0/k_B$. The optimal bias voltage V_0 is determined by the point at which the minimum detectable energy intersect the thermally-driven motion.

III. NANOSCALE BOLOMETER

A second major project is aimed at the development of nanoscale bolometers, with the potential for substantially increased sensitivity to infrared light in the frequency range of 0.1-10 THz. A bolometer consists of a volume whose temperature is changed by absorbing infrared light, and a thermistor element that detects the changes in temperature. The volume has a heat capacity \mathcal{C} , a thermal conductance to the temperature bath \mathcal{G} , and a corresponding thermal time constant $\tau = \mathcal{C}/\mathcal{G}$. The minimum detectable radiated power, called the noise equivalent power (*NEP*) is set by thermal fluctuations through the thermal conductance, and is equal to $NEP = \sqrt{4k_B T^2 \mathcal{G}}$. Operating at lower temperatures with smaller thermal conductances leads to smaller values of the *NEP*.

There is however a quantum limit to the minimum achievable thermal conductance, first predicted theoretically [10–13] and later verified experimentally [14]. For a thermal conductance formed by a nanoscale wire, this quantum limit is achieved at low temperatures and is given by

$$\mathcal{G}_Q = \frac{4\pi^2 k_B^2 T}{3h}, \quad (13)$$

where h is Planck's constant. The corresponding limit to the noise equivalent power is given by

$$NEP = \left(\frac{16\pi^2 k_B^3 T^3}{3h} \right)^{1/2}. \quad (14)$$

At a temperature of 100 mK, this corresponds to 5×10^{-19} W/Hz^{1/2}; at 20 mK this is 4×10^{-20} W/Hz^{1/2}, values that are 10-100 times smaller than is presently achievable.

Even smaller values should be achievable by engineering the thermal link that provides the conductance \mathcal{G} . The quantum limit (13) is achieved for a straight wire with unity phonon transmissivity; conductances smaller than this can be achieved by engineering the phonon dispersion relation for transmission through the conductance. We have completed calculations that indicate that a periodically modulated structure, forming a phononic bandgap, can for a range of temperatures achieve a thermal conductance significantly less than the quantum limit [15]. An example of such a structure and its dispersion relation is shown in Fig. 6.

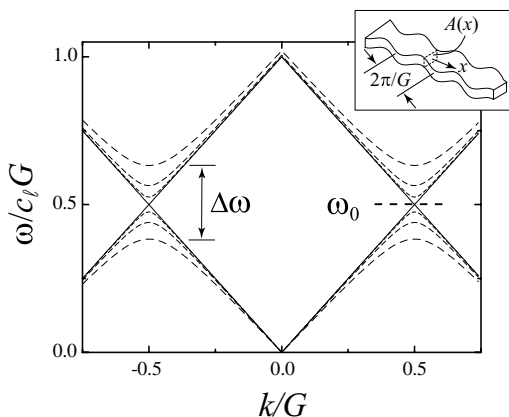


FIG. 6: Calculated dispersion relation for different modulation strengths, using a longitudinal acoustic model. The gap $\Delta\omega$ is indicated, as is the bandgap center frequency ω_0 .

The corresponding calculation for the thermal conductance, in units of the quantum of thermal conductance, is shown in Fig. 7.

Structures such as these may prove useful in tuning and adjusting the thermal conductance of nanoscale structures.

We are presently fabricating and characterizing a nanometer-scale bolometer, for which we use a mechanically suspended volume of semi-insulating GaAs, which is patterned using electron-beam lithography to define a

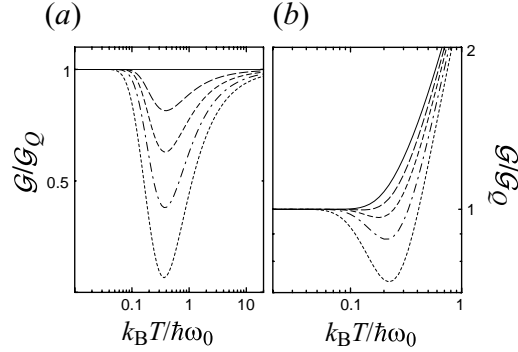


FIG. 7: (a) Calculated thermal conductance in units of the quantum of thermal conductance \mathcal{G}_Q , for one mode of a phononic crystal beam, as a function of temperature normalized to the bandgap center ω_0 . The solid line is for a simple beam, showing the quantum value $\mathcal{G}/\mathcal{G}_Q = 1$, and the dotted lines are for phononic crystal beams with bandgap widths $\Delta\omega/\omega_0 = 0.2, 0.4, 0.6$ and 1 . (b) Thermal conductance including the higher order modes, for the simple beam (solid line) and for the same series of modulation widths $\Delta\omega/\omega_0$.

volume, $2 \times 3 \times 0.2 \mu\text{m}^3$, suspended by thin, $4 \times 0.2 \times 0.2 \mu\text{m}^3$ legs from the bulk substrate. The thermistor element is a aluminum-aluminum oxide-copper-aluminum oxide-aluminum tunnel (SINIS) junction, fabricated on the surface of the GaAs. The volume of copper normal metal is $3 \times 0.3 \times 0.04 \mu\text{m}^3$, and the tunnel characteristics of the junction are sensitive to the temperature of the electrons in this normal metal. A electron micrograph and sketch of the structure appears in Fig. 8. This structure has a heat capacity approximately 10^4 times smaller than micromachined bolometers, and we anticipate bolometric sensitivity of order 100 times higher than in these other bolometer designs [16–18].

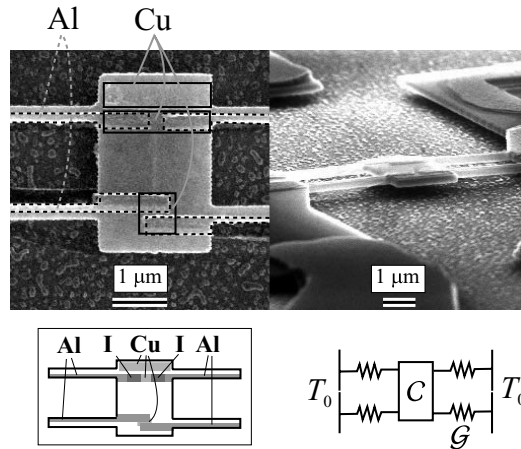


FIG. 8: Electron micrograph of a nanoscale bolometer, comprising a pair of Al-I-Cu-I-Al (SINIS) tunnel junctions fabricated on the surface of a $2 \times 3 \times 0.2 \mu\text{m}^3$ GaAs block, which is suspended by four $0.2 \times 0.2 \times 4 \mu\text{m}^3$ beams from the bulk substrate. Below is a sketch of the geometry including the tunnel junctions, and a highly simplified thermal model, indicating the heat capacitance \mathcal{C} of the central block (dominated by that of the normal Cu metal), and thermal conductance \mathcal{G} for each of the four beams.

A set of low temperature differential conductance curves as a function of bias voltage are shown for one of the SINIS tunnel junctions, showing the very strong temperature dependence of the zero-bias conductance, and at the lowest temperature a fairly well-defined superconducting gap $\Delta = 180 \mu\text{V}$ per junction. In tunnel junctions with large volumes of normal metal, the gap structure is defined by large peaks in the conductance at $\pm\Delta$, which are missing here; we believe this is due to very weak electron-phonon coupling in these structures, which causes excessive heating of the normal metal electrons at non-zero bias; this question is still under investigation.

However, the zero-bias conductance is found to be well described by the conventional BCS theory for NIS tunnel junctions (see e.g. Solymar [19]). The non-equilibrium situation at non-zero bias can be phenomenologically explained using a hot-electron model, where the electrons in the normal metal are thermally decoupled from the phonons; this effect is fairly well understood in fully three dimensional phonon systems, i.e. in bulk insulating substrates, but the situation when the substrate has a strongly reduced geometry as here is less clear. Calculations indicate that for phonons in a fully three dimensional system, the effective electron-phonon thermal conductance scales as the fifth power of the electron temperature T_{el}^5 , while in an effectively one-dimensional phonon system, such as applies here at the lowest temperatures, the electron-phonon conductance should scale as T_{el}^4 .

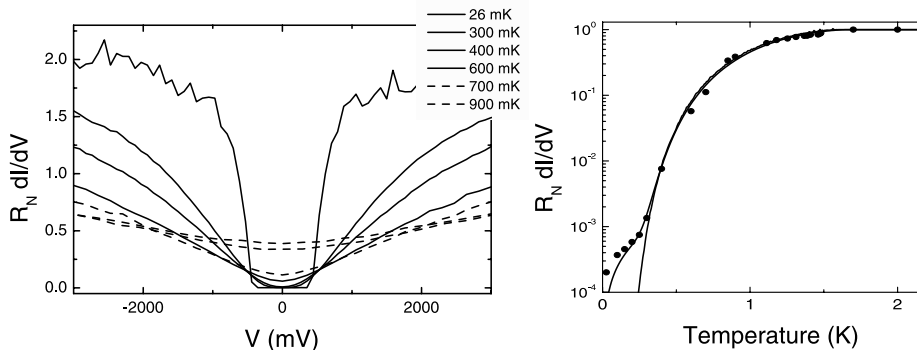


FIG. 9: (left) Conductance as a function of bias voltage for a suspended SINIS tunnel junction, measured at a series of temperatures from 25 mK to 900 mK. (right) Zero-bias conductance as a function of temperature, showing a good match to the predictions of classical BCS theory.

Measurements of the electrical readout noise of the SINIS thermistor elements yields a temperature sensitivity of $6 \mu\text{K}/\sqrt{\text{Hz}}$ at an operating temperature of 100 mK; we estimate the thermal time constant τ to be $4 \mu\text{sec}$. The corresponding estimate for the electrical noise-limited NEP is $2 \times 10^{-18} \text{ W}/\text{Hz}^{1/2}$ at 100 mK, within about a factor of 5 of what we expect. This bolometer should be able to detect single 1 THz photons with a signal-to-noise of unity; we are presently attempting to couple signals optically to verify whether this is the case.

IV. FABRICATION TECHNIQUES

Our integrated structures are fabricated through a combination of electron-beam lithography, metal deposition, anisotropic reactive ion-beam etching, and isotropic wet etching. In Fig. 10 we display the major steps associated with a GaAs-based structure definition. We start with heterostructure substrate, comprising a bulk, semi-insulating GaAs substrate, a sacrificial AlGaAs layer $0.4 \mu\text{m}$ thick, and a top semi-insulating GaAs structural layer $0.2 \mu\text{m}$ thick. This heterostructure is grown on a bulk GaAs substrate using molecular beam epitaxy (MBE), and can be designed with different layer sequences, thicknesses, and so on.

We then begin patterning the structure. We use conventional electron beam lithography to pattern a poly-methyl methacrylate bilayer (PMMA), comprising a 495 KD molecular weight bottom layer and a 960 KD weight top layer, the PMMA dissolved in an anisole solvent. Each layer is spun on at 3 krpm for 45 seconds and baked for 10 minutes at 180°C . The pattern is exposed with a scanning electron microscope configured for lithography; the electron beam dosage is about $350 \mu\text{C}/\text{cm}^2$, with a beam voltage of 35 kV. After exposure, we develop the pattern in a 1:3 methyl isobutyl-ketone:isopropyl alcohol (MIBK:IPA) developer, and rinse in IPA. The use of the PMMA bilayer, with a lower resolution underlayer and higher-resolution top layer, yields a undercut resist profile which gives a high-yield metal and insulator liftoff. We then thermally evaporate a layer of SrF_2 (strontium fluoride), an insulating material that has a fairly low sublimation point, lifts off well, and is partially water-soluble. The SrF_2 layer ranges from 10-100 nm in thickness, depending on subsequent steps. Following the evaporation, the unwanted SrF_2 is lifted off with the PMMA by soaking for several minutes in acetone.

The SrF_2 provides an excellent mechanical mask for the subsequent anisotropic reactive-ion etching of the GaAs and AlGaAs substrate material. We use a commercial parallel-plate reactive ion etcher, and flow pure Cl_2 gas at a pressure of 5 mtorr and a flow rate of 10 sccm. An rf power of 150 W generates a self-biased plasma

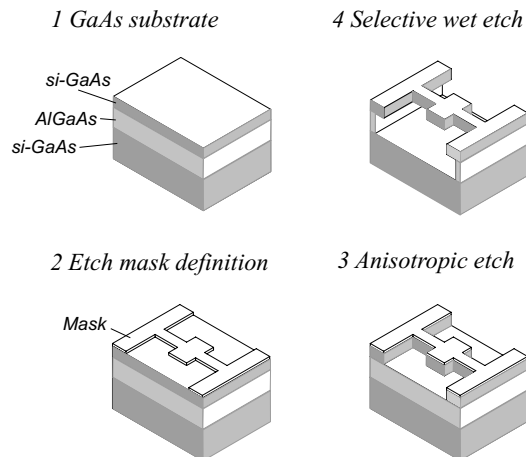


FIG. 10: Suspended heterostructure definition, starting (1) with a GaAs heterostructure substrate, (2) patterning an etch mask, (3) anisotropic etch of the GaAs and AlGaAs layers and (4) sacrificial wet etch, suspending the final structure.

voltage of about 350 V, and yields a GaAs and AlGaAs etch rate of about $0.1 \mu\text{m}/\text{min}$. The etch is carried out to a depth corresponding to complete etching of the exposed GaAs and AlGaAs layers, typically $0.6 \mu\text{m}$, ending on the bottom, bulk GaAs layer. The SrF_2 mask is not noticeably etched by this process, and the SrF_2 can then be removed by soaking in distilled water for 2-3 minutes.

Following this step, the exposed AlGaAs can be removed using either concentrated hydrochloric acid or a dilute (10%) solution of hydrofluoric acid; these acids do not noticeably etch GaAs, leaving the structural layer intact. The etch time varies with the size of the desired, final suspended structure. For the structure we use for the bolometer design above, etch times of order 1-2 minutes are appropriate.

The nanoscale tunnel junctions are patterned on the surface of the suspended structure. These tunnel junctions can comprise either aluminum-aluminum oxide-aluminum tunnel junctions, which below the superconducting transition temperature of Al (about 1.5 K for thin-film aluminum) forms a superconductor-insulator-superconductor (SIS) tunnel junction, or copper-aluminum oxide-aluminum tunnel junctions which are normal metal-insulator-superconductor (NIS) junctions below 1.5 K. Aluminum is an excellent material for fabrication of such structures on the deep sub-micron scale, because it forms finely-grained thin films that are fairly stable in air, and its oxide is thermally and mechanically stable, providing a high-voltage tunnel barrier for tunnel junctions. The challenge in fabricating nanoscale tunnel junctions is that the trilayer (metal-metal oxide-metal) structure must be defined in a single vacuum cycle in order to achieve high reliability structures. This can be achieved either by unpatterned, bulk trilayer deposition of the two metal films and intermediate oxide layer, which is subsequently patterned to form the tunnel junction structures, or by using a suspended resist bridge technique to pattern the films as they are deposited, and using different evaporation angles to achieve the geometric differentiation. We have followed the latter approach, which is sketched out in Fig. 11.

We spin-coat the substrate with a bottom layer of the copolymer methyl methacrylate and a top layer of 960 KD molecular weight PMMA, the first spun at 2 krpm for 45 seconds followed by a 10 minute 180°C bake, the second at 3 krpm for 45 seconds followed by the same 180°C bake. Exposure is done by electron-beam lithography at 35 kV with a $350 \mu\text{C}/\text{cm}^2$ dosage; develop is in 1:3 MIBK:IPA with an IPA rinse. The co-polymer is extremely sensitive to the electron beam dosage, and overdevelops approximately $0.3\text{-}0.5 \mu\text{m}$ laterally beyond the edge of the exposed pattern. This significantly undercuts the top PMMA layer and allows us to use the directional nature of thermal evaporation to define the tunnel junctions, as shown in Fig. 11.

Once the suspended bridge pattern has been defined, we fabricate the tunnel junction by placing the structure in a thermal evaporator, and pumping the chamber out to a few times 10^{-7} torr. The substrate is then tilted by an angle of $20\text{-}25^\circ$ with respect to the line of sight to the evaporation crucible, and a thin film (30-100 nm) of Al is evaporated from a W crucible. The Al film is then oxidized by admitting a small pressure (~ 10 mtorr) of pure oxygen to the chamber, and waiting from 10-100 seconds to achieve the correct oxide thickness. The substrate is then tilted to -20° to -25° with respect to the line of sight, and a second metal film (either aluminum for an SIS tunnel junction, or copper for a NIS tunnel junction) is evaporated. The completed structure is then

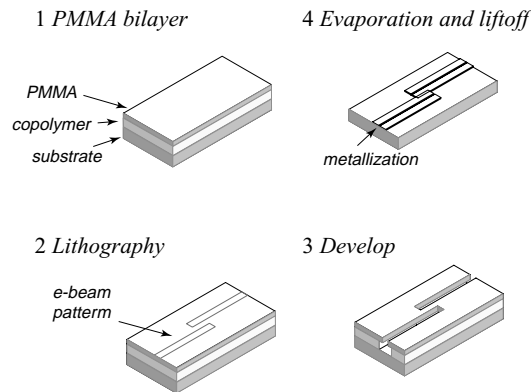


FIG. 11: Fabrication sequence for angled metal tunnel junctions; in step (1), a bilayer resist is spun and baked on the substrate, in (2) the electron beam lithography pattern is written, in (3) the pattern developed out, and in (4) metal evaporations are carried out at two angles, defining the tunnel junction in the center of the pattern.

removed from the evaporator and liftoff completed in acetone. Tunnel junction areas can range from 0.01-0.3 μm^2 , depending on the particular pattern and the tilt angles, and tunnel junction resistances range from 100 Ω to 10 M Ω , depending on the junction area and oxidation time. Areas are highly repeatable, and junction resistances tend to reproduce to within a factor of two, other factors being the same.

We are also pursuing a quite different, parallel approach to integrated electromechanical devices. This approach uses GaAs substrates that include a buried two-dimensional electron gas in the top structural layer; the two-dimensional electron gas can be contacted through diffused ohmic contacts to measure transport characteristics, and can be gated using lithographically patterned electrostatic top gates that allow the lateral definition of the electron gas in the two-dimensional sheet. This approach has been used to define single quantum dots in the electron gas as well as double quantum dots, the latter allowing extremely sensitive spectroscopic probing of the electrons' electrical environment (see e.g. [20]). We have been pursuing the development of such structures to allow probing of the vibrational environment, by embedding a double quantum dot structure in a mechanically suspended structure. An example of the types of structures we are fabricating is shown in Fig. 12.

The authors acknowledge the support provided by a NASA Explorer Award No. ECS-9980734, the Army Research Office under Contract No. DAAD-19-99-1-0226, the National Science Foundation under the XYZ-On-A-Chip program, and by a Research Corporation Research Innovation Award.

-
- [1] A.N. Cleland and M.L. Roukes. Fabrication of high frequency nanometer scale mechanical resonators from bulk Si crystals. *Appl. Phys. Lett.*, 69:2653–2656, 1996.
 - [2] A.N. Cleland, M. Pophristic, and I. Ferguson. Single-crystal aluminum nitride nanomechanical resonators. *Applied Physics Letters*, in press, 2001.
 - [3] K. Wang, A.C. Wong, and C.T. Nguyen. VHF free-free beam high-Q micromechanical resonators. *J. Microelectromechanical Systems*, 9:347–360, 2000.
 - [4] A.N. Cleland and M.L. Roukes. Noise processes in nanomechanical resonators. *submitted to Phys. Rev. B*, 2001.
 - [5] A.N. Cleland and M.L. Roukes. Nanometer scale mechanical electrometry. *Nature*, 320:160–161, 1998.
 - [6] R. Schoelkopf, P. Wahlgren, A.A. Kozhevnikov, P. Delsing, and D.E. Prober. The radio-frequency single-electron transistor (rf-set): A fast and ultrasensitive electrometer. *Science*, 280:1238–1242, 1998.
 - [7] M.P. Blencowe and M.N. Wybourne. Sensitivity of a micromechanical displacement detector based on the radio-frequency single electron transistor. *App. Phys. Lett.*, 77:3845–3847, 2000.
 - [8] K. Schwab. Quantum measurement with nanomechanical systems. *Proceedings of the International Conference on Quantum Computation, Sydney, Australia*, 2001.
 - [9] M. Devoret and R. Schoelkopf. Amplifying quantum signals with the single-electron transistor. *Nature*, 406:1039–1046, 2000.
 - [10] D.E. Angelescu, M.C. Cross, and M.L. Roukes. *Superlattices and Microstruct.*, 23:673, 1998.
 - [11] L.G.C. Rego and G. Kirczenow. Quantized thermal conductance of dielectric quantum wires. *Phys. Rev. Lett.*,

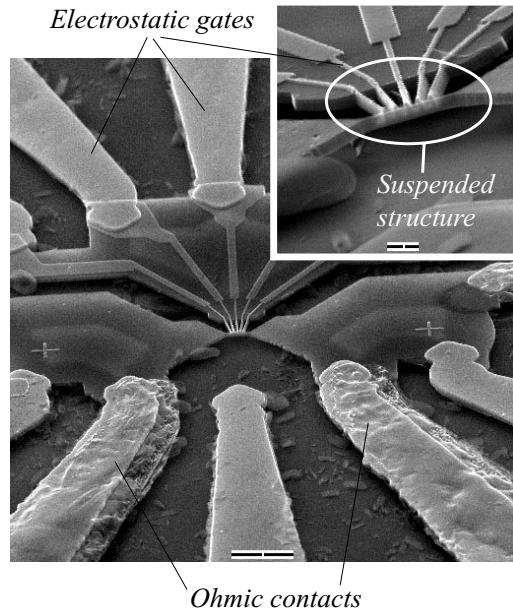


FIG. 12: GaAs structure including an embedded two-dimensional electron gas. Drain-source leads and electrostatic gates are shown in the large scale picture, and the inset shows a higher-magnification view of the suspended structure with integrated gates.

81:232–235, 1998.

- [12] M.P. Blencowe. Quantum energy flow in mesoscopic dielectric structures. *Phys. Rev. B*, 59:4992–4998, 1999.
- [13] D.H. Santamore and M.C. Cross. Effect of surface roughness on the universal thermal conductance. *Phys. Rev. B*, 63:184306, 2001.
- [14] K. Schwab, E.A. Henriksen, J.M. Worlock, and M.L. Roukes. Measurement of the quantum of thermal conductance. *Nature*, 404:974–977, 2000.
- [15] A.N. Cleland, D.R. Schmidt, and C.S. Yung. Thermal conductance of nanostructured phononic crystals. *to be published in Phys. Rev. B*, 2001.
- [16] P.M. Downey, A.D. Jeffries, and S.S. Meyer et al. *Appl. Opt.*, 23:910, 1984.
- [17] J.W. Zhou, K. Farooqui, P.T. Timbie, G.W. Wilson, C.A. Allen, S.H. Moseley, and D.B. Mott. Fabrication of submicron high-aspect ratio GaAs resonators. *Proc. 1995 IEEE MTT-S Intl. Microwave Symp. (Orlando FL)*, pages 1347–1350, 1995.
- [18] P.D. Mauskopf, J.J. Bock, H. Del Castillo, W.L. Holzapfel, and A.E. Lange. *Appl. Opt.*, 36:765, 1997.
- [19] L. Solymar. *Superconductive Tunnelling and Applications*. Wiley-Interscience, New York, 1972.
- [20] T.H. Oosterkamp, L.P. Kouwenhoven, A.E.A. Koolen, N.C. van der Vaart, and C.J.P.M. Harmans. Photon sidebands of the ground state and first excited state of a quantum dot. *Phys. Rev. Lett.*, 78:1536, 1997.